Geochimica et Cosmochimica Acta Vol. 54, pp. 781–795

0016-7037/90/$3.00 + .00

Cerium anomalies in lateritic profiles

JEAN-JACQUES BRAUN,[1] MAURICE PAGEL,[2] JEAN-PIERRE MULLER,[3] PAUL BILONG,[4] ANNIE MICHARD,[5] and BERNARD GUILLET[6]

[1]Centre de Pédologie Biologique, CNRS, BP 5, 54501 Vandœuvre-lès-Nancy, Cedex, France
[2]CREGU and GS CNRS-CREGU, BP 23, 54501 Vandœuvre-lès-Nancy, Cedex, France
[3]ORSTOM, Département T.O.A. and Laboratoire de Minéralogie-Cristallographie, UA CNRS 09, Universités Paris 6 et 7, 4 place Jussieu, 75252 Paris Cedex 05, France
[4]Département des Sciences de la Terre, Faculté des Sciences de l'Université de Yaoundé, BP 812, Yaoundé, Cameroun
[5]Laboratoire de Géochimie Isotopique, Centre de Recherches Pétrographiques et Géochimiques, CNRS, 54501 Vandœuvre-lès-Nancy Cedex, France
[6]Laboratoire de Géologie de la Matière Organique, UA CNRS 724, Université d'Orléans, BP 6759, 45067 Orléans Cedex 2, France

(*Received May* 31, 1989; *accepted in revised form December* 15, 1989)

Abstract—The REE geochemistry and mineralogy have been studied in four lateritic profiles, one derived from a syenite (Akongo, SW Cameroon), the others being developed on a gneissic basement and located along a soil toposequence (Goyoum, E Cameroon). There is a fractionation between LREE and HREE in the lateritic samples during weathering, the weathered residual products being enriched in LREE (from La to Eu) and depleted in HREE (from Gd to Lu); sampled waters are enriched in HREE in relation to the syenite host-rock. A positive Ce-anomaly has been found systematically at the top of the saprolite, beneath a zone of iron oxide accumulation in the laterite. Up to 2000 ppm Ce may be present. In the Akongo profile, cerianite, CeO_2, is present as very fine coatings in non-ferruginous clayey domains. Primary REE-bearing accessory minerals are weathered at the bottom of the profile. Specifically, allanite and apatite are transformed into florencite and rhabdophane but these phases have no Ce-anomaly. All the data are interpreted as the result of the following processes: (1) REE leaching in a reducing environment, (2) oxidation of Ce^{3+} to Ce^{4+} in an oxidizing environment, and (3) deposition of cerium as cerianite whereas the other REE remain in solution.

INTRODUCTION

THE RARE EARTH ELEMENTS (REE) have very similar chemical properties which tend to vary gradually along the group. During weathering processes, the chemical behavior of REE depends on several factors including Eh, pH, the presence in soil of organic and inorganic ligands (CANTRELL and BYRNE, 1987), exchange sites on clays (AAGAARD, 1974; ROALDSET, 1974), mineralogical distribution of REE in the parent material, and especially the nature of the host rock-accessory minerals association. BALASHOV et al. (1964), RONOV et al. (1967), NESBITT (1979), DUDDY (1980), and TOPP et al. (1984) have shown that REE are fractionated during weathering processes, the weathered residual products being enriched in light REE (from La to Eu) and depleted in heavy REE (from Gd to Lu).

Among the REE, cerium is especially interesting to study because it can occur in nature as Ce^{3+} like the majority of lanthanides, or as Ce^{4+} in oxidizing conditions. If soluble Ce^{3+} is oxidized to Ce^{4+}, it precipitates from solution as very insoluble CeO_2. Consequently, the solution shows a negative Ce-anomaly.

Ce-anomalies are well known in the marine environment. The existence of Ce^{4+} in sea water has been invoked to explain, on the one hand, the negative Ce-anomaly in sea water (GOLDBERG, 1961; DE BAAR et al., 1988), and on the other hand, the positive Ce-anomaly in manganese nodules (ELDERFIELD et al., 1981; PIPER, 1974).

In the continental environment, the geochemistry of cerium is poorly documented. A positive Ce-anomaly has been found in some weathering profiles on various types of source-rocks. In lateritic ferricretes (iron crusts) which form on amphibolites, basaltic breccia, and gabbros from the Ivory Coast, STEINBERG and COURTOIS (1976) have found pronounced positive Ce-anomalies. BONNOT-COURTOIS (1981) has also observed a positive Ce-anomaly on a lateritic soil developed on the Korhogo granite (Ivory Coast). RANKIN and CHILDS (1976) have described a preferential enrichment of cerium related to Mn-Fe concretions in a New-Zealand lateritic soil. In a contrary case, TRESCASES et al. (1986) have observed a major negative Ce-anomaly related to the accumulation of strongly Ce-depleted lanthanite $[(LREE)_2(CO_3)_3 8H_2O]$ in a fossilised lateritic profile dating from the Pleistocene. Based on our literature survey, it seems that the nature of secondary minerals incorporating the REE, and especially Ce, is not known. The main mineral containing Ce^{4+} is cerianite (CeO_2) but its occurrence in nature has rarely been reported. An interesting case is represented in the Afu Hills (Nigeria) where the breakdown of bastnäesite $[Ce_2La_{1.5}(Nd,Pr)_{0.5}(CO_3)]$ and the weathering of fluocerite $[Ce_2La_{1.5}(Nd,Pr,Th)_{0.5}F_{12}]$ in oxidizing conditions lead to the formation of La-bastnäesite and cerianite $[(Ce^{4+},Th)O_2]$ (STYLES and YOUNG, 1983). Cerianite is also present as a weathering product in the Poços de Caldas area (Brazil) (FRONDEL and MARVIN, 1959).

From the above studies, it is not clear where and how Ce occurs in lateritic environments and which physicochemical parameters control Ce accumulation. To assess the distribution of cerium, we have selected several lateritic profiles from Cameroon which are representative of the main lateritic weathering profiles in the tropical zone (MILLOT, 1964; NAHON, 1987). These profiles have formed on two parent-rocks with different REE contents. One profile, previously studied

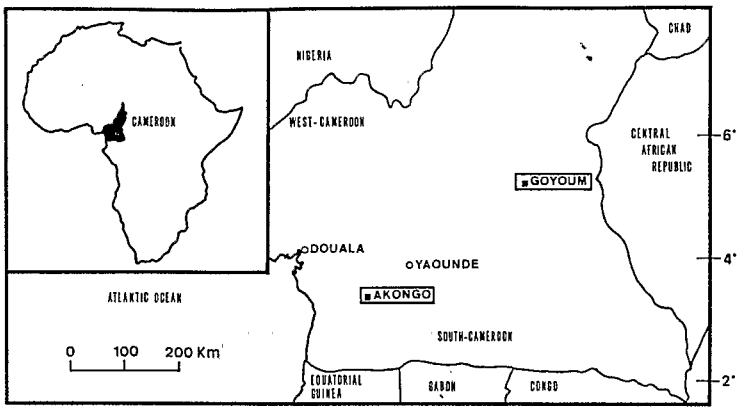

FIG. 1. Location of the two areas studied.

in detail by BILONG (1988), contains ferricrete which developed on an alkaline syenite in the Akongo area (SW Cameroon; Fig. 1). The three others are loose and nodular lateritic profiles which were studied by MULLER (1987) and are located in the Goyoum area (E Cameroon; Fig. 1). These latter profiles belong to a soil toposequence which formed on a gneissic basement and represent a more general case of lateritic weathering encountered in Central Africa under a humid tropical climate and forest cover (BOCQUIER et al., 1984).

PETROGRAPHIC AND MINERALOGICAL FEATURES OF THE PROFILES AND MATERIALS

Description of the parent materials and the profiles

The fresh gneiss and syenite were never encountered in the studied pits. Samples of fresh rocks used as references for geochemical study were therefore collected in less weathered syenitic or gneissic boulders located in lower parts of the profiles. The major features of the studied profiles in both localities are described below.

Ferricrete from Akongo. The sampled site is situated at the top of a syenitic hill. The syenite of the Akongo site belongs to the syenite group of the Lolodorf-Akongo axis (South-Cameroon) (EDIMO, 1985). Samples collected from the Akongo pit show a granular structure with a slight mineral orientation determined by amphibole, pyroxene and some biotite crystals. The major minerals are perthite, albite, green amphibole, clinopyroxene, biotite, and magnetite. The accessory minerals are zircon, titanite, apatite, and abundant green allanite. Monazite is rarely encountered within the Akongo pit syenite samples. The studied profile is five meters deep and shows four different horizons (Fig. 2). From the bottom to the top, the profile consists of the following:

1. A saprolite, 130 cm thick, which preserves the preexisting rock structure and texture. It is a sandy saprolite which is friable and porous. Microscopic analysis shows that the main weathering products are large booklets of pseudomorphous kaolinite derived

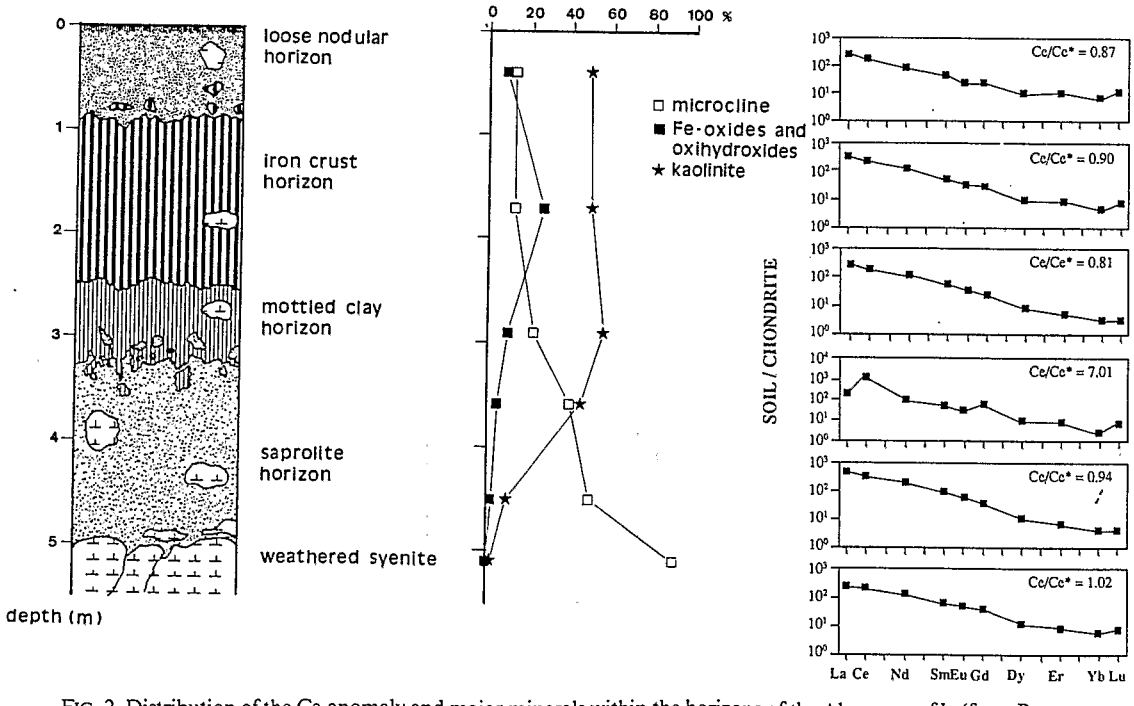

FIG. 2. Distribution of the Ce-anomaly and major minerals within the horizons of the Akongo profile (from BILONG, 1988).

from the weathering of biotite and microcline, associated with tiny crystals of halloysite, iron oxide (hematite), and oxihydroxide (goethite). Residual primary minerals such as microcline (80% of the unweathered primary phase) and magnetite persist in the saprolite. However, these minerals show weathering features along cracks. Crystals of amphibole, epidote, and biotite are present within the less weathered syenitic sand. The saprolite contains 1 to 4 cm thick, anastomosed, white clayey subhorizontal seams (S) which envelop the sandy domains where weathered syenitic boulders are present. These seams are composed of halloysite and residual microcline crystals and are characterized by a dense fissural porosity between close halloysitic aggregates. Their boundaries with the loose sandy syenite are marked by thin iron oxides coatings. SEM observations show that the pore walls between and within the aggregates are composed of halloysite needles about 1 μm length showing a geodic growth. The saprolite shows a gradual, undulating and discontinuous upper limit.

2. A mottled clay horizon, 75 cm thick, consisting of juxtaposed red decimetric and white centimetric domains. The red domains (RD) are soft, isolated ferruginous mottles in which the parent rock texture can be still recognized. Hematite (~11% Fe_2O_3 in whole rock) and kaolinite are the main constituents. White domains (WD) are soft and mainly composed of kaolinite. The upper limit of this horizon is undulating.
3. An iron crust, 230 cm thick, composed of a purple-red, ferruginous and indurated material crossed by a network of ochre-yellow and white, soft, clayey and porous spots. In this layer, the parent-rock structure and texture have completely disappeared. The upper limit is gradational.
4. A loose nodular ferruginous horizon in which indurated hematitic nodules are surrounded by a yellowish brown, mainly kaolinitic, material. Near the surface, organic matter accumulates down to 5 cm.

Loose and nodular lateritic profiles from Goyoum. The parent rock of the Goyoum profiles is a fine-grained orthogneiss which shows an oblique foliation with regard to the topographic surface. Veins of much darker rock, rich in biotite, are enclosed in the leucocratic main body of the rock. The major minerals are quartz, biotite, muscovite, oligoclase, and microcline. Garnet is a minor mineral and the accessory minerals are apatite, rutile, zircon, xenotime, and monazite (SARAZIN et al., 1982; and present study). The three studied profiles are located along the upper part of a soil toposequence (Fig. 3; MULLER and BOCQUIER, 1986). Pits, 10 to 12 meters deep, exhibit three main horizons which cut the oblique foliation of the gneiss. The main horizons are the following from bottom to top:

1. A thick, friable, and porous saprolite preserving the original structure of the gneiss. Microscopic analysis shows that the weathered products are mainly composed of large booklets of kaolinite, which follow the original foliation of the rock, and iron oxides and oxihydroxides (hematite and goethite; ~10% Fe_2O_3 in whole rock). The remaining parent minerals are quartz, muscovite, and accessory minerals such as zircon and monazite. In the upper part, saprolite is embedded in red and yellow clayey materials in which the rock structure is no longer observed. The clayey material consists of small platelets of kaolinite associated with iron oxides and oxihydroxides (~10% Fe_2O_3).
2. A loose nodular ferruginous horizon in which two types of indurated and mainly hematitic nodules are recognized: large and irregular nodules (20–80 mm in diameter) in which the original texture of the gneiss can be still recognized and marked by large booklets of kaolinite (1–50 μm in length), and small (less than 20 mm in diameter) subrounded nodules in which the gneissic texture is absent and in which small platelets of kaolinite (<1 μm) are randomly distributed. These nodules are embedded in a mixture of clay minerals and iron oxides and oxihydroxides, which appear

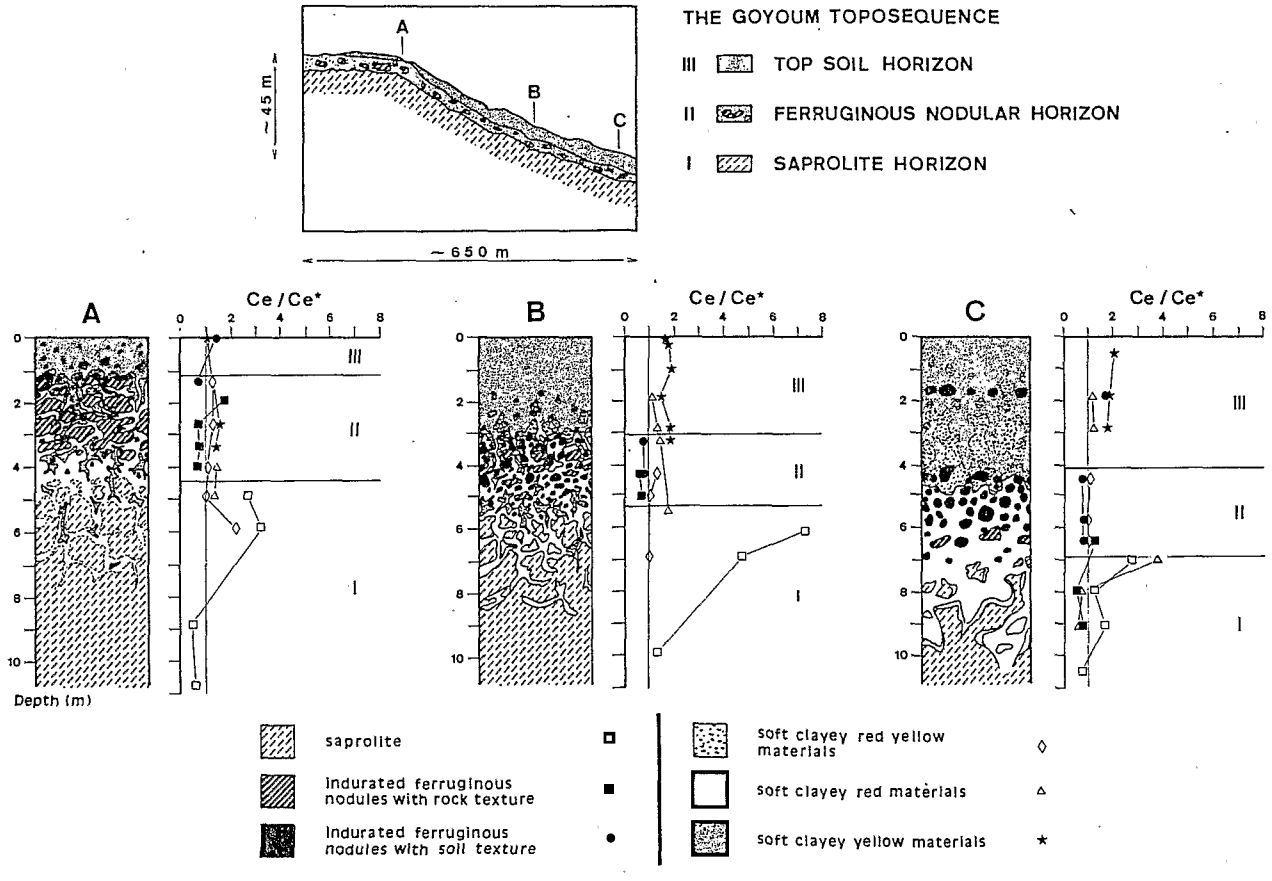

FIG. 3. Distribution of the Ce-anomaly within the Goyoum profiles. The description of the profiles is issued from MULLER (1987).

redder (hematite more abundant than goethite) and more compact than that found at the top of the saprolite. This red material shows a diffuse boundary with a red yellowish loose material (goethite ≫ hematite), which is increasingly abundant towards the top of the nodular zone and appears as a roughly network of interconnected fissures. The upper limit of this horizon is marked by a sharp boundary of the ferruginous nodules.

3. A topsoil horizon (sometimes called an "oxic" horizon), mainly kaolinitic, which consists of a red to yellow clay-sized matrix. From the bottom to the top, the red material from the underlying horizon progressively occurs in discontinuous masses (soft nodules) and disappears at around one meter depth. Organic matter is present down to 20 cm.

It is important to point out that the relative extensions of these three zones depend strongly on the topographic position of the profile (Fig. 3): the upper profile A shows a diminished topsoil horizon whereas this horizon is more developed and the saprolite occurs at a greater depth within profiles B and C.

ANALYTICAL TECHNIQUES AND SAMPLING

Analytical techniques

Several analytical techniques have been used to characterize the minerals containing REE and especially Ce.

Petrographic observations, densimetric separations of accessory minerals and their weathering products, and water analysis have been performed only on samples from the Akongo site.

Undisturbed soil samples were collected in the different horizons. After impregnation with epoxy resin, samples were thin-sectioned and polished, and studied by scanning electron microscopy (STEREOSCAN 250 CAMBRIDGE coupled with a PGT SYSTEM III energy dispersive spectrometer). Backscattered electron imaging was used. Quantitative elemental analysis was done with an automated CAMEBAX SX50 microprobe analyser. An accelerating voltage of 15 kV, a specimen current of 10.10^{-9} A and an electron beam focused to approximately 1 μm were used throughout. All measurements were made using a 30 sec livetime couting time period. Data processing was carried out using the PAP program (POUCHOU and PICHOIR, 1984). The limit of detection is approximately 0.2 wt% element for the elements reported here.

Ultra-thin sections of the Ce-enriched zones of the white seams have been studied by transmission electron microscopy (PHILIPS 420 TEM/STEM coupled with a LINK AN 10000 energy dispersive spectrometer). The electron diffraction patterns were obtained from a sample area about 0.17 μm^2.

Heavy REE-bearing minerals of the 50–200 μm particle-size fraction of the saprolite and weathered syenite were separated by densimetric and magnetic methods. Heavy minerals grains were observed by SEM and REE contents were analysed with the CAMEBAX SX 50. Florencite in the heavy mineral fraction of the weathered syenite was analyzed by x-ray diffraction with $CuK_{\alpha 1}$ radiation at a scanning speed of 2θ/min.

REE of water from the marsh located between Akongo hills were analyzed by isotope dilution with a 206 SA CAMECA mass spectrometer at CRPG (Nancy) following the method of MICHARD et al. (1983). One pore-water and two surface-waters were analyzed.

The amount of REE in soil and weathered rock samples of Akongo and Goyoum was determined by ICP (JY 48P Spectrometer) at CRPG (Nancy) using the GOVINDARAJU and MEVELLE (1987) method. Powdered soil or rock samples were decomposed by fusion with $LiBO_2$. The fusion products were dissolved in a complexing acid solution which was passed through cation-exchange column in which only the REE are fixed. The resins were then washed with HNO_3 (2 M) to remove all elements other than the REE. The REE are eluted with 7.25 M HNO_3 and analyzed by ICP.

Soil sampling

Akongo profile. Two successive samplings were performed. The first sampled the five main horizons of the pit. In this case, REE contents are average values for each horizon. The second was a more detailed sampling of the saprolite and mottled horizon during a second mission to the Akongo site. The latter sampling was conducted according to colors of the different horizon zones (these colors represent either Fe-oxide accumulation or Fe impoverished zones), and according to the main features of the horizon structures (especially white seams).

Goyoum profiles. Twenty to thirty samples from the various materials described above have been collected from pits in each of the three profiles studied.

Water sampling

Water was sampled at the end of the dry season. This water represents drainage from three syenitic hills. The method used to collect pore water is similar to that described by HESSLEIN (1976) and SARAZIN et al. (1976). The principle is based on the equilibration of the chemical potential on both sides of a permeable membrane which limits a container filled with distilled water and placed in sediments during 15 days. Fresh water was sampled with a Swinnex Millipore® 0.2 μm microfiltration system. Water was preserved in acidic conditions by addition of two drops of concentrated HNO_3.

RESULTS

REE distribution in the Akongo and Goyoum profiles

The concentrations of ten REE are listed in Table 1. $(La/Yb)_{ch}$ and Ce/Ce* ratios have been calculated. The chondrite-normalized patterns along the Akongo profile are reported in Fig. 2. The patterns exhibit LREE enrichment relative to HREE as shown by $(La/Yb)_{ch}$ ratio which varies from 40 to 100. A significant Ce-anomaly (Ce/Ce* = 7.01) appears at the upper part of the saprolite, just beneath the iron oxide accumulation zone [mottled clay horizon overlain by iron crust, BILONG (1988)]. Up to 810 ppm of Ce have been found. It can be seen in Fig. 2 that this positive Ce-anomaly does not correspond to the maximum of the weathering products.

The variation of Ce/Ce* as a function of depth and nature of materials within the profiles from Goyoum are shown in Fig. 3. REE contents, Ce/Ce*, and La/Yb ratios are reported in Table 2. The patterns exhibit a less pronounced LREE enrichment relative to HREE ($(La/Yb)_{ch}$ varying from 3 to 13). However, as in the Akongo profile, the positive Ce-anomaly is again situated at the top of the saprolite, just below the iron-oxide accumulation zone (ferruginous nodular horizon), regardless of the location of the profile on the slope and the relative thickness of the different horizons [Ce/Ce* is close to 4 in the top profile (A) and the bottom profile (C), and is about 8 in the middle-slope profile (B)].

Detailed REE distribution in the lower part of the Akongo profile

In order to get deeper insight in the way the REE distribution and especially the Ce-anomaly are related to the type of materials, more detailed observations have been carried out at the transition between saprolite and iron-oxide accumulation zone of the Akongo profile which exhibits both the highest Ce content and Ce-anomaly (Fig. 4). Syenite-normalized REE patterns are presented according to the different color zones of the lower (LS) and upper (US) part of the saprolite and according to the different materials and structures such as white domains (WD) and red domains (RD) of the lower part of the mottled clayey-ferruginous horizon, and white clayey seams (S). A chondrite-normalized REE pattern

Table 1 : Concentrations of ten REE (ppm) from the Akongo lateritic profile (from BILONG, 1988).
Ce-anomaly = $Ce/Ce^* = (3Ce_{sn}/Ce_{sn}) / (2La/La_{sn} + Nd/Nd_{sn})$
Also listed are $(La/Yb)_{sn} = (La/La_{sn})/(Yb/Yb_{sn})$ ratio which indicates the REE fractionation.

	La	Ce	Nd	Sm	Eu	Gd	Dy	Er	Yb	Lu	ΣREE	$(La/Yb)_{ch}$	Ce/Ce*
loose nodular horizon	67.90	129.71	46.64	7.16	1.65	5.87	2.74	1.72	1.23	0.29	264.91	41	0.87
iron crust	70.67	141.42	52.42	7.75	1.83	6.30	2.33	1.35	0.72	0.18	284.97	72	0.90
mottled clay zone	62.64	116.67	57.27	8.89	2.15	5.25	2.21	0.90	0.57	0.09	256.64	81	0.81
saprolite (top)	49.78	810.18	47.38	6.95	1.80	12.13	2.40	1.38	0.45	0.17	932.62	81	7.01
saprolite (bottom)	94.80	206.98	91.30	14.35	3.39	7.58	2.94	1.04	0.69	0.10	423.17	101	0.94
weathered syenite	53.65	132.63	64.81	10.45	2.83	7.90	3.27	1.44	1.02	0.21	278.21	39	1.02

Table 2 : Concentrations of ten REE (ppm) from the Goyoum profiles. $(La/Yb)_{ch}$, Ce/Ce* are explained in Table 1.

Profil A	depth (m)	La	Ce	Nd	Sm	Eu	Gd	Dy	Er	Yb	Lu	ΣREE	$(La/Yb)_{ch}$	Ce/Ce*
●	0.05	8.98	28.62	6.78	1.87	0.54	1.60	1.61	0.97	1.08	0.24	52.29	6.1	1.43
★	0.05	31.09	73.98	25.71	5.46	1.07	4.42	4.74	2.74	3.12	0.44	152.77	7.3	1.05
●	1.35	11.05	20.08	9.05	2.50	0.64	2.11	2.44	1.41	1.48	0.29	51.05	5.5	0.80
◊	1.35	17.34	49.45	14.12	3.23	0.79	2.70	2.73	1.58	1.81	0.30	94.05	7.0	1.26
■	1.95	9.32	38.21	7.85	2.08	0.65	2.01	2.28	1.34	1.41	0.24	65.39	4.9	1.80
■	2.65	16.87	26.05	12.21	2.66	0.95	2.20	2.24	1.17	1.20	0.24	65.79	10.3	0.70
◊	2.65	12.59	37.92	10.03	2.16	0.39	1.79	1.81	1.00	1.15	0.18	69.02	8.0	1.34
★	2.65	38.55	140.38	33.45	6.89	1.46	5.70	4.79	2.61	2.94	0.43	237.20	9.6	1.60
■	3.35	9.88	18.72	10.07	2.45	0.64	2.16	2.79	1.67	1.80	0.30	50.48	4.0	0.81
★	3.35	22.61	79.59	20.81	3.95	0.81	3.12	3.26	1.86	2.09	0.29	138.39	8.0	1.53
■	3.95	10.91	18.63	10.65	2.77	0.96	2.61	3.06	1.78	1.88	0.32	53.57	4.3	0.73
◊	3.95	22.63	57.78	21.33	4.22	0.88	3.48	4.09	2.37	2.68	0.36	119.82	6.2	1.10
△	3.95	34.41	117.05	31.50	6.34	1.46	5.29	5.29	3.05	3.40	0.48	208.27	7.4	1.48
□	4.85	39.00	223.25	21.89	4.77	1.40	4.86	4.70	2.87	3.21	0.53	306.48	8.9	2.67
◊	4.85	36.04	90.68	26.46	5.30	1.29	4.52	4.31	2.52	2.91	0.49	174.52	9.1	1.13
△	4.85	34.69	111.61	28.61	5.92	1.39	4.86	5.02	2.92	3.39	0.43	198.84	7.5	1.42
□	5.85	19.18	136.29	12.97	2.85	1.03	2.96	2.60	1.44	1.65	0.26	181.23	8.5	3.23
◊	5.85	17.13	87.21	14.57	3.24	0.76	3.12	3.25	1.94	2.26	0.38	133.86	5.6	2.24
□	8.85	35.95	41.21	26.96	5.67	0.79	4.71	5.22	2.70	3.04	0.44	126.69	8.7	0.51
□	10.75	45.60	60.42	37.80	7.87	1.25	5.97	4.81	2.22	2.54	0.38	168.86	13.2	0.58
Profil B														
★	0.05	11.43	40.64	9.70	2.61	0.41	2.72	3.58	2.37	2.78	0.35	76.59	3.0	1.56
★	0.15	13.62	48.85	11.67	3.04	0.42	2.95	4.09	2.65	3.13	0.44	90.86	3.2	1.57
★	0.30	12.64	46.97	11.21	2.66	0.59	2.64	3.79	2.42	2.88	0.41	86.21	3.2	1.62
★	1.05	23.09	99.11	16.36	4.70	1.15	4.73	3.56	2.53	2.86	0.56	158.65	5.9	1.94
△	1.90	25.43	77.58	23.44	6.76	1.53	6.07	5.25	3.58	4.08	0.73	154.45	4.6	1.32
★	1.90	27.84	94.87	23.96	6.70	1.35	5.94	4.46	2.97	3.31	0.60	172.00	6.2	1.49
△	2.85	23.44	70.50	17.98	5.13	0.93	5.10	4.40	3.07	3.46	0.68	134.69	5.0	1.34
★	2.85	26.78	110.67	21.64	5.88	1.29	5.74	4.45	3.02	3.44	0.65	183.56	5.7	1.83
●	3.25	14.44	24.71	11.39	2.71	0.72	2.16	2.15	1.35	1.49	0.28	61.40	7.1	0.76
△	3.25	26.13	84.12	19.73	5.54	1.23	5.45	4.41	3.05	3.47	0.71	153.84	5.5	1.44
★	3.25	25.48	106.68	21.09	5.87	1.33	5.86	4.41	3.01	3.49	0.68	177.90	5.4	1.85
●	4.25	17.06	27.03	14.52	3.05	1.02	2.67	2.74	1.72	1.96	0.28	72.05	6.4	0.70
■	4.25	17.95	32.33	16.22	3.81	1.09	3.22	3.75	2.23	2.50	0.42	83.52	5.3	0.78
◊	4.25	26.14	76.35	19.49	5.39	1.29	5.16	4.16	3.00	3.39	0.69	145.06	5.7	1.31
■	4.95	17.39	27.69	18.86	4.28	0.78	3.57	4.76	2.90	3.34	0.39	83.96	3.8	0.67
●	4.95	19.75	30.62	20.76	4.97	1.08	4.14	4.66	2.75	3.51	0.56	92.80	4.1	0.66
◊	4.95	25.05	63.06	19.06	5.35	1.35	5.13	4.54	3.20	3.66	0.69	131.09	5.0	1.13
△	5.45	30.37	123.59	26.60	7.23	1.62	7.04	5.92	3.99	4.54	0.83	211.73	4.9	1.78
□	6.05	8.58	147.20	8.57	2.12	0.52	2.88	2.42	1.69	1.92	0.28	176.15	3.3	7.32
□	6.85	15.74	174.92	16.48	3.87	0.95	4.23	4.03	2.54	2.94	0.42	226.12	3.9	4.70
◊	6.85	18.38	44.72	17.61	4.25	0.90	3.88	4.99	2.94	3.31	0.49	101.47	4.1	1.05
□	9.85	15.48	50.35	15.67	3.78	0.62	3.57	4.42	2.67	3.05	0.41	100.02	3.7	1.39
Profil C														
★	0.55	21.91	97.99	17.92	3.84	0.63	3.71	3.94	2.51	2.94	0.47	155.86	5.5	1.98
●	1.85	14.29	55.50	13.76	3.15	0.78	2.51	2.43	1.29	1.43	0.22	95.36	7.3	1.67
△	1.85	35.35	99.74	35.19	7.28	1.22	5.64	5.56	3.33	3.85	0.58	197.74	6.7	1.21
★	1.85	36.70	151.32	36.41	7.79	1.44	6.29	5.76	3.31	3.78	0.56	253.36	7.1	1.76
△	2.85	40.85	110.47	40.68	8.13	1.67	6.21	5.78	3.33	3.89	0.58	221.59	7.7	1.16
★	2.85	36.71	144.55	34.20	6.99	1.19	5.89	5.56	3.30	3.80	0.56	242.75	7.1	1.70
●	4.40	30.33	47.79	24.98	5.35	1.02	4.12	3.42	1.73	1.81	0.29	120.84	12.3	0.70
◊	4.40	41.36	96.24	36.07	7.03	1.30	5.41	4.89	2.75	3.05	0.46	198.56	10.0	1.02
●	5.65	27.28	48.15	22.44	5.00	0.98	3.82	3.30	1.69	1.81	0.37	114.84	11.1	0.78
◊	5.65	35.96	72.24	30.43	5.99	1.11	4.72	4.70	2.72	3.03	0.42	161.32	8.7	0.88
■	6.35	17.87	46.60	17.01	3.86	0.94	3.10	3.39	2.16	2.45	0.40	97.78	5.4	1.12
●	6.35	23.29	44.47	19.02	4.62	1.02	3.59	4.25	2.65	2.97	0.53	106.41	5.8	0.84
◊	6.35	33.83	82.53	28.27	5.47	1.24	4.35	4.25	2.51	2.79	0.42	165.66	8.9	1.08
□	6.95	19.52	122.96	17.74	3.97	1.25	3.91	4.92	3.32	3.95	0.57	182.11	3.6	2.74
△	6.95	30.47	258.18	27.24	5.57	1.21	5.75	5.32	3.28	3.78	0.52	341.32	5.9	3.69
□	7.85	21.57	57.83	20.07	4.19	1.19	3.71	4.15	2.97	3.53	0.50	119.71	4.5	1.16
■	7.85	23.31	35.23	24.51	4.96	1.09	3.70	3.89	2.50	2.98	0.48	102.65	5.7	0.64
△	7.85	33.89	54.75	29.78	6.29	1.25	5.23	6.23	3.96	4.55	0.60	146.53	5.5	0.71
□	8.95	22.38	80.35	20.18	4.42	1.46	4.10	4.38	2.61	3.09	0.47	143.44	5.3	1.56
■	8.95	23.33	38.46	23.38	5.45	1.30	4.47	5.93	4.47	5.78	0.84	113.41	3.0	0.70
△	8.95	31.92	46.97	28.67	6.41	1.28	5.27	6.66	4.20	4.74	0.66	136.78	5.0	0.64
□	10.35	29.89	45.53	29.26	6.53	1.27	5.37	6.25	3.91	4.63	0.62	133.26	4.7	0.65

□ saprolite
■ indurated ferruginous nodules with rock texture
● indurated ferruginous nodules with soil texture
◊ soft clayey red yellow materials
△ soft clayey red materials
★ soft clayey yellow materials

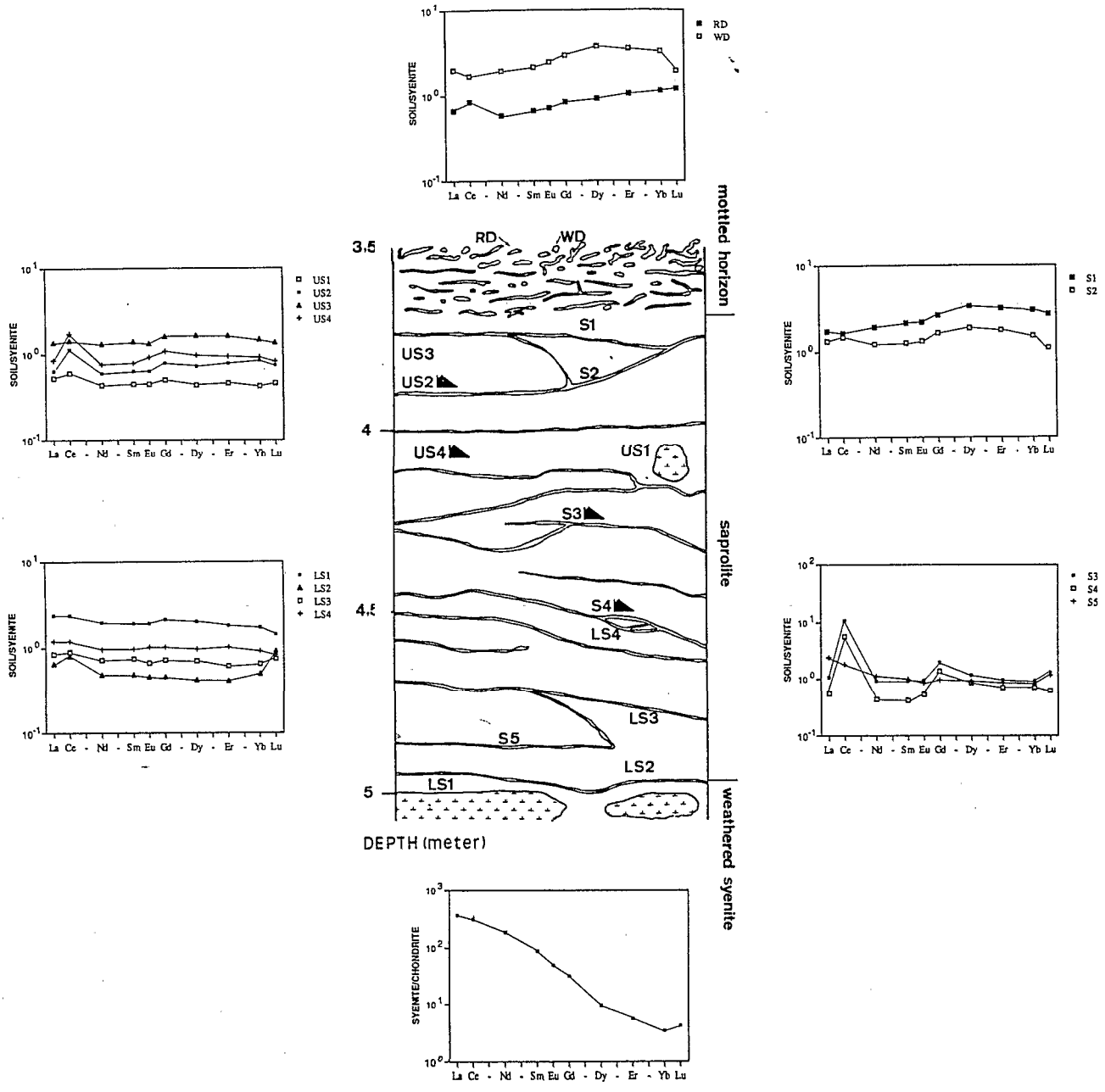

FIG. 4. Detailed REE distribution in the lower part of the Akongo profile. Syenite-normalized patterns are reported with regard to the location of the zones within the profile. Chondrite-normalized pattern is indicated for the weathered syenite. ▲: location of the Ce-anomaly for samples having a Ce/Ce* > 1.5.

is presented for the weathered syenite (WS). REE contents, $(La/Yb)_{ch}$, $(La/Yb)_{sy}$, and Ce/Ce* ratios of the same samples are reported in Table 3.

As with the majority of igneous rocks, the syenite from the Akongo-Lolodorf group does not show a Ce-anomaly. Chondrite-normalized patterns for ten fresh syenite samples are presented in Fig. 5 (from EDIMO, 1985). The REE contents vary widely from syenite to syenite. These syenites show an enrichment in LREE. Ce/Ce* ratio is close to one and the $(La/Yb)_{ch}$ ratio varies from 50 to 80. The chondrite-normalized pattern for the studied weathered syenite shows a similar strong fractionation of REE ($(La/Yb)_{ch}$ = 100) and no Ce-anomaly (Ce/Ce* = 1.01).

The syenite-normalized patterns of selected samples are discussed in relation to their shape. Five significant types of patterns can be distinguished (Fig. 4):

1. Flat patterns either without or with a very slight LREE enrichment with respect to the weathered syenite (LS1, LS3, LS4, US3). Ce/Ce* is about 1 and $(La/Yb)_{sy}$ varies from 0.90 to 1.30. The REE content of the different zones which are either higher or lower than those of the weathered syenite corresponds to a different distribution of the REE-bearing minerals in the parent rock.
2. LREE-enriched pattern (S5) with Ce/Ce* ratios close to 0.85 and the $(La/Yb)_{sy}$ ratio close to 3.

Table 3 : Concentrations of ten REE (ppm) from the different colour and structure zones of the Akongo lateritic profile (saprolite horizon and lower part of the mottled clay horizon). Ce/Ce*, $(La/Yb)_{ch}$ are explained in Table1.
Also listed are $(La/Yb)_{sy} = (La/La_{sy})/(Yb/Yb_{sy})$ ratio which indicates the REE fractionation related to the weathered syenite (WS).

	La	Ce	Nd	Sm	Eu	Gd	Dy	Er	Yb	Lu	ΣREE	$(La/Yb)_{ch}$	$(La/Yb)_{sy}$	Ce/Ce*
WS	82.05	196.77	88.47	13.24	2.88	6.72	2.51	0.97	0.60	0.11	394.21	101	1.00	1.01
LS1	193.52	469.28	175.14	25.26	5.58	14.16	5.05	1.77	1.03	0.16	890.79	138	1.37	1.05
LS2	52.78	157.05	42.19	6.31	1.29	3.03	1.05	0.40	0.30	0.10	264.40	129	1.29	1.32
LS3	70.10	172.35	63.21	9.73	1.94	4.87	1.75	0.59	0.39	0.08	324.93	132	1.31	1.07
LS4	98.37	233.85	84.99	12.59	2.95	6.87	2.43	0.99	0.54	0.09	443.58	134	1.33	1.04
US1	42.76	118.45	37.74	5.81	1.27	3.36	1.07	0.45	0.25	0.05	211.16	126	1.25	1.21
US2	51.94	220.28	52.51	8.23	1.82	5.18	1.79	0.76	0.50	0.08	343.01	76	0.76	1.81
US3	111.39	279.06	118.14	18.44	3.86	10.82	4.09	1.57	0.89	0.15	548.26	92	0.92	1.06
US4	69.24	341.19	67.25	10.30	2.64	7.19	2.43	0.90	0.55	0.09	501.69	93	0.92	2.12
S1	141.70	324.79	169.71	28.64	6.40	17.90	8.53	3.09	1.80	0.30	702.56	58	0.58	0.94
S2	110.03	294.07	108.89	16.75	3.80	10.88	4.66	1.74	0.90	0.12	551.72	90	0.89	1.14
S3	90.98	2106.00	81.84	12.17	2.84	13.59	2.95	0.96	0.56	0.15	2311.89	119	1.19	10.08
S4	44.74	1101.89	37.64	5.53	1.54	9.28	2.14	0.68	0.43	0.07	1203.87	76	0.76	10.84
S5	203.01	364.32	101.97	13.35	2.45	6.58	2.35	0.83	0.49	0.13	695.35	305	3.03	0.85
RD	54.90	164.16	51.40	8.76	2.07	5.66	2.29	1.00	0.68	0.13	290.92	59	0.59	1.29
WD	162.41	329.08	171.03	28.30	7.11	19.63	9.40	3.40	1.98	0.21	732.34	60	0.60	0.86

3. Patterns with positive Ce- and Gd-anomalies (S3, S4). The positive Ce-anomaly is very significant (Ce/Ce* = 10). Gd/Gd* is about 2.
4. Patterns with a weak positive Ce-anomaly (Ce/Ce* ratios from 1.3 to 2). The other REE are not fractionated when compared to the weathered syenite ($0.8 < (La/Yb)_{sy} < 1.3$). This type of REE distribution is found either close to the weathered syenite (LS2) or at the top of the saprolite within sandy matrix with well-preserved syenite structure (US1, US2, US4).
5. HREE-enriched patterns with a weak negative or positive Ce-anomaly (Ce/Ce* varying from 0.9 to 1.5 for S1, S2, RD, WD).

Therefore, the Ce-anomaly is heterogeneously distributed within the upper half of the saprolite. This anomaly seems to be most pronounced within (1) the sandy saprolitic material from the top of the saprolite and (2) some clayey white seams which show both the highest Ce-contents (1100 and 2100 ppm) and the highest Ce/Ce* ratios (about 10).

Weathering petrography

SEM observations have been made on thin-sections of the parent-material and on the lower and upper part of the saprolite, and on some grains about 50–200 μm in size separated from both the weathered syenite (WS) and the lower part of the saprolite (LS1) by densimetric and magnetic methods (Figs. 6, 7, 8). TEM observations have been made on ultra-thin sections of Ce enriched zones of halloysitic seams. These observations allow us to follow the evolution of major and REE-bearing accessory minerals as well as the formation of secondary phases during weathering.

Primary mineral weathering

Major minerals:

1. Microcline. Among the major minerals, microcline is the most stable. It shows slight weathering along cracks which are filled with kaolinite. It remains as relatively fresh crystals within the saprolite.

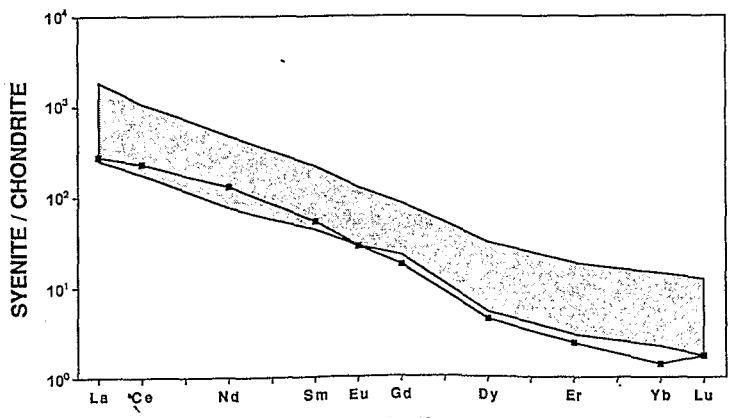

FIG. 5. Range of REE contents of ten Akongo syenite samples (from EDIMO, 1985). Ce/Ce* = 1 and $(La/Yb)_{ch}$ varies from 50 to 80. (■) represents the Akongo pit sample where $(La/Yb)_{ch}$ is about 100 and Ce/Ce* = 1.

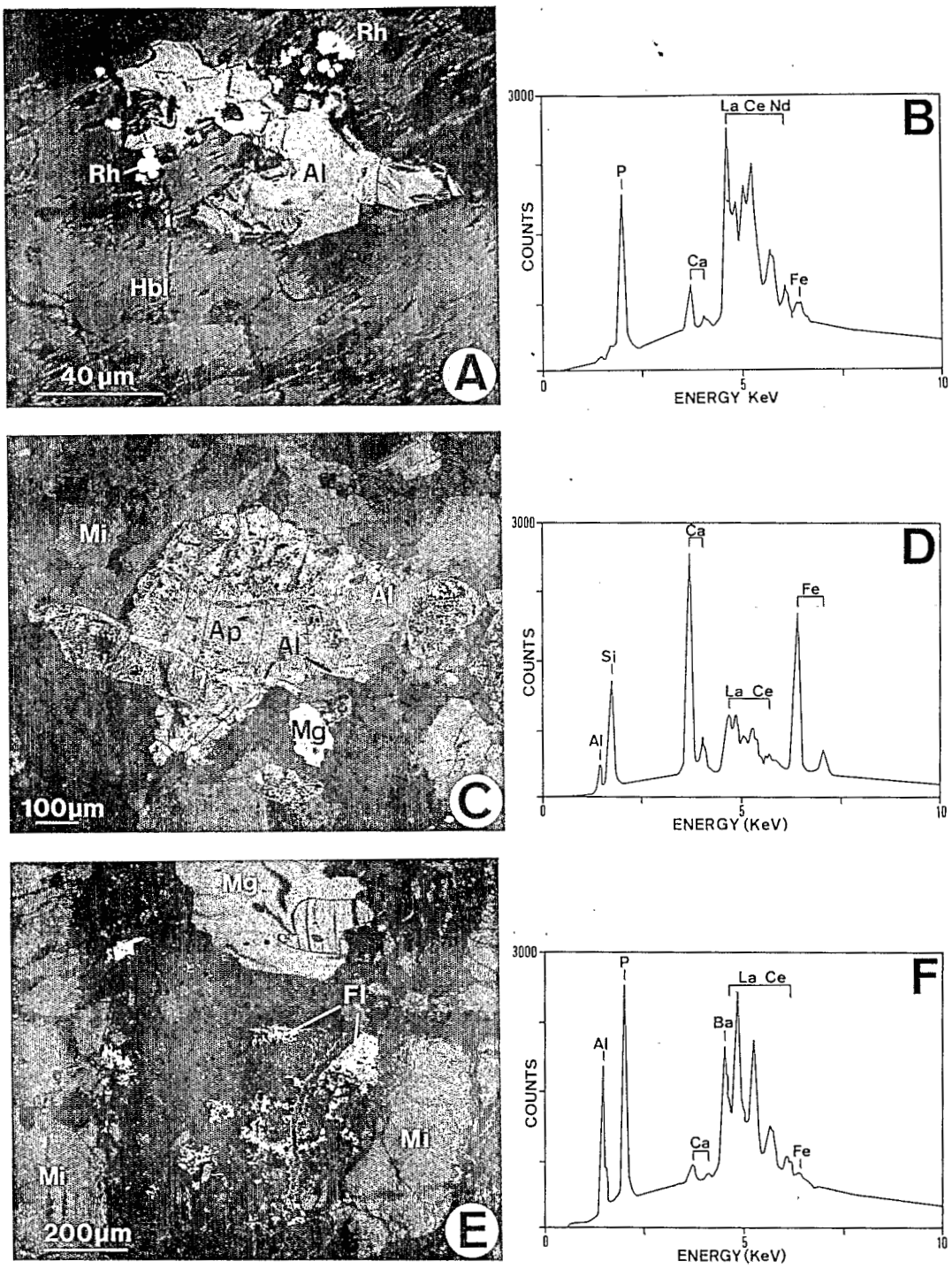

FIG. 6. A—Crystal of allanite (Al) which shows REE-enriched zones (indicated by arrows) and rounded rhabdophane crystals (Rh) included in a hornblende crystal (Hbl), (SEM-backscattered electrons).

B—Energy dispersive pattern of a rhabdophane crystal.

C—Thin-section view (SEM-backscattered electrons) of a weathered apatite crystal (Ap) containing allanite crystals (Al). This thin-section was prepared from the least Akongo syenite sample.

D—Energy dispersive pattern of an allanite crystal.

E—Thin-section view (SEM-backscattered electrons) of an apatite grain relict composed of aggregated florencite donuts (Fl). These aggregates are crossed by clayey zones remembering the shape of the allanite crystals included in apatite grains shown on the figure 6C. Neighbors are unweathered microcline (Mi) and magnetite crystals (Mg). This thin-section proceeds from a more weathered syenite sample.

F—Energy dispersive pattern of a florencite donut.

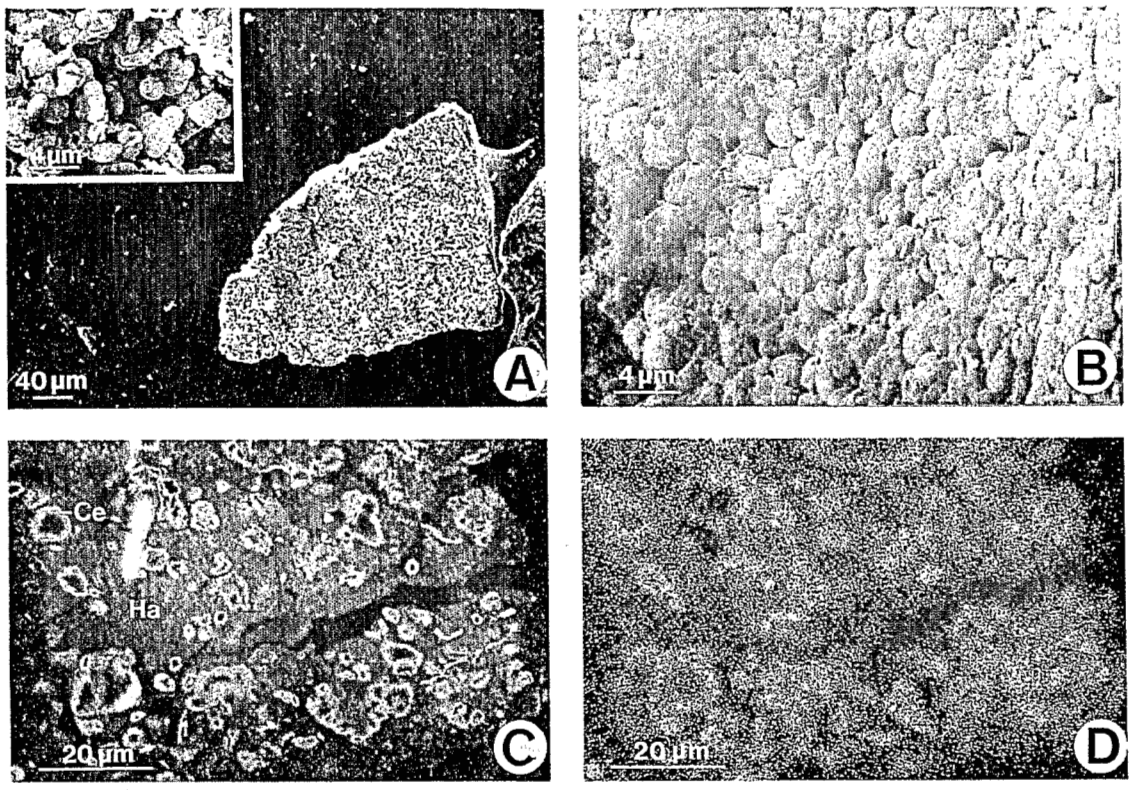

FIG. 7. A—A completely weathered grain composed only of florencite donuts. This grain has been selected by densimetric and magnetic fractionation. A detail of its surface is also shown (SEM-secondary electrons).
B—Detailed view of the surface of a florencite aggregate showing the characteristic "donut" shape of the florencite grains (SEM-secondary electrons).
C—Filling of pores by cerianite (Ce) in a halloysitic seam (Ha) of the upper part of the saprolite (SEM-secondary electrons).
D—X-ray element map of Ce from the same area shown in micrograph 7D.

2. Pyroxene and hornblende. These disappear entirely in the upper saprolite with goethite and hematite pseudomorphs after them. The biotite crystals are weathered into large kaolinite booklets.
3. Magnetite. The crystals are very abundant and occur, within the saprolite, with slight weathering features such as cracks. They are progressively fractured and then destroyed.

REE-bearing accessory minerals:

1. Zircon and sphene. Zircon grains (about 100–200 μm length) are rounded. The sphene crystals are weathered within the saprolite and anatase (TiO_2) is formed.
2. Allanite and apatite. Allanite (Fig. 6B) is the most abundant LREE-bearing mineral in the syenite. The grains, about 50–100 μm in diameter, are evenly distributed in the rock and are associated either with hornblende (Fig. 6A) or with apatite crystals (500 μm to 1 mm length) as shown on Fig. 6C, where allanite crystals are included in a large apatite grain. Although allanite grains are very abundant in the weathered syenite and the lower part of the saprolite, they are absent in upper part. Apatite is observed only in the less weathered syenite, in which the grains show some cracks and large voids (Fig. 6C). The weathering products are rare small rounded crystals (5–10 μm in diameter) of rhabdophane ($LREEPO_4H_2O$) (Fig. 6D) and widespread florencite [$REEAl_3(PO_4)_2(OH)_6$] (Fig. 6F). The relicts of apatite grains (200–600 μm), which are observed in the more weathered rock sample and in the syenitic sand (LS1) either on thin-sections (Fig. 6E) or on magnetically selected grains (Fig. 7A and B), are transformed into florencite which has been identified by X-ray diffraction. The florencite grains have a "donut"-like shape about 2–4 μm in diameter and form highly porous aggregates. Florencite donuts are similar to those described by SAWKA et al. (1986) on weathering products of Lachlan Fold Belt granite (Australia). These aggregates are crossed by clayey zones (Fig. 6E) which trace the location of the allanite crystals previously located into the apatite. Occurrences of isolated crystals or chains of florencite donuts have also been observed. These isolated crystals are more hydrated and the Al content is higher than in aggregated grains, according to microprobe analysis (37% compared to 28% of Al_2O_3). REE analysis in aggregated and isolated crystals show no Ce-anomaly but there is a depletion of LREE from La to Sm (Fig. 9) in crystals with high aluminum contents. Thorium is often associated with the REE within the same accessory minerals. A thorianite

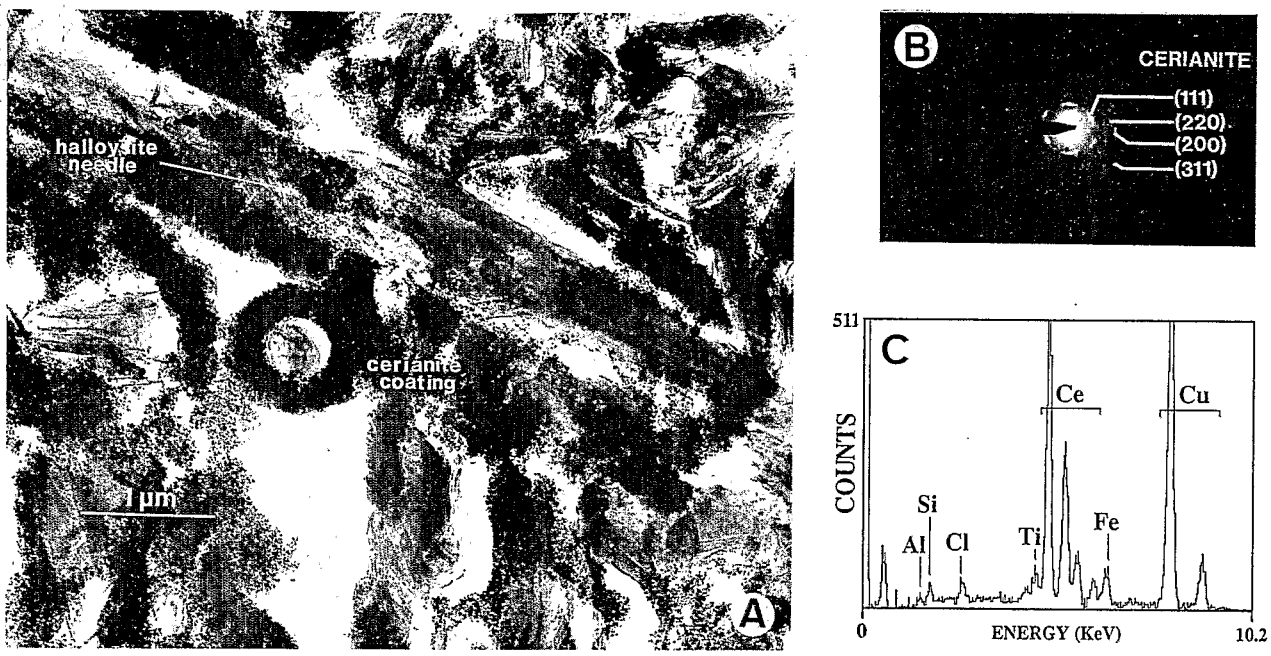

FIG. 8. A— Halloysite needles with cerianite coating (TEM).
B— Electron diffraction pattern of cerianite.
C— Energy dispersive pattern of cerianite.

(ThO_2) crystal about 10 μm in diameter has also been observed in the weathered syenite.

Occurrence of cerianite. Cerianite is observed without a systematic relationship to primary REE-bearing phases. In the Ce-enriched clayey white seams located in the upper part of the saprolite (S4), cerianite has been identified by X-ray diffraction and electron diffraction (Fig. 8B). Electron microprobe analysis and dispersive energy pattern (Fig. 8C) indicate that cerium is the only REE present with Al, Si and a small amount of Fe. La, Sm, Nd, and Th are beneath the detection limit of the electron microprobe. The highest CeO_2 content is 37 wt% (Fig. 10). The Ce content is higher near the pore walls and decreases towards the clayey zones. Cerianite and halloysite fill some seam pores as shown in Fig. 7C and D. The electron image (Fig. 8A) shows the very fine-grained cerianite crystals coating the halloysite needles (1–10 μm in length). The cerianite grains have a slight orientation as indicated by the diffuse spots on the electron diffraction pattern (Fig. 8B).

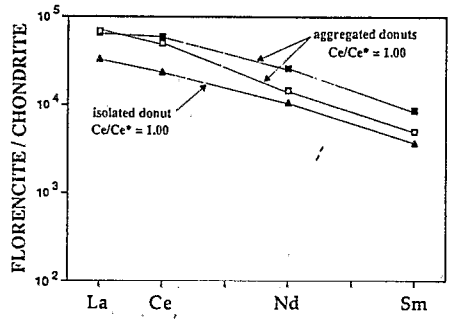

FIG. 9. Chondrite-normalized patterns for microprobe analysis of aggregated and isolated donuts of florencite.

Water analysis

The chondrite-normalized REE patterns of the pore water and the two surface water samples are shown in Fig. 11. LREE contents (Table 4) in the pore water are 20 times that of the surface water while Fe^{2+} contents, determined by ICP, are 100 times greater (2 mg/l in surface water, 250 mg/l in pore water). ELDERFIELD and SHOLKOVITZ (1987) have observed a similar increase of REE contents in pore water from reducing nearshore sediments of Buzzard Bay with respect to

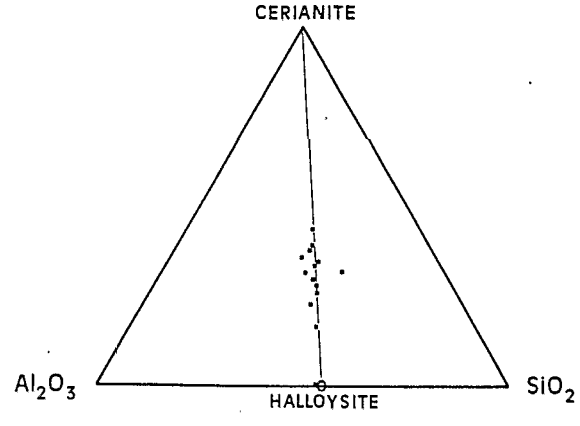

FIG. 10. Microprobe analysis results for CeO_2, Al_2O_3, and SiO_2 from several Ce-enriched zones located within white seams are reported on a ternary diagram to show that there is a admixing between two minerals phases: cerianite and halloysite.

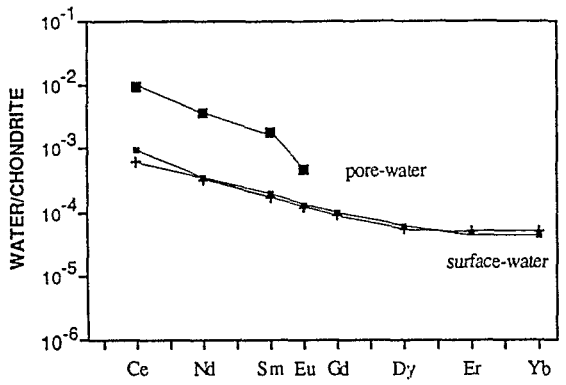

FIG. 11. Chondrite-normalized patterns for the pore water and the surface water samples.

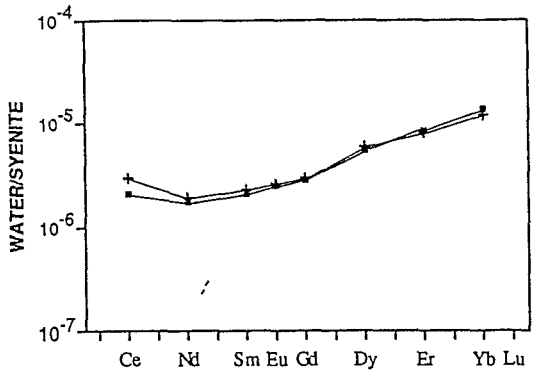

FIG. 12. Syenite-normalized patterns for the two surface water samples showing the HREE enrichment with regard to syenite.

the REE content of seawater. Syenite-normalized patterns for the surface water show that it is enriched in HREE (Fig. 12).

DISCUSSION

REE behavior within lateritic profiles

General trends. According to NESBITT (1979) and HUMPHRIS (1984), the mobilization of the REE during weathering processes results from different factors related to the parent rock mineralogy, specifically the distribution of the REE in the primary bearing minerals, the stability of these minerals during weathering, and their abundance in the parent material. It is generally agreed that LREE are less mobile than HREE and there is a consequent enrichment in the LREE relative to the HREE in the soil samples. The La/Yb ratio is generally used to quantify this fractionation. If we consider EDIMO's (1985) data for the Akongo syenite, the different zones of the lateritic profile exhibit a pronounced fractionation (Figs. 2 and 4). The weathered syenite and the sandy matrix of the saprolite show a relative LREE enrichment ($(La/Yb)_{ch}$ of 100 to 140), whereas an increase of HREE content relative to LREE is observed in the white seams of the top of the upper part of the saprolite, the mottled horizon, the iron crust, and the nodular horizon ($(La/Yb)_{ch}$ ratios of 80 to 40). The syenite-normalized patterns (Fig. 4) of the white seams and the bottom of the mottled horizon show a net increase of HREE, which may be due to the accumulation of HREE-bearing grains such as zircon while LREE included in less resistant minerals such as allanite and apatite are leached away and accumulated as florencite or rhabdophane in other parts of the profile. Therefore, among the mobilized REE, the major part of the LREE is rapidly precipitated as secondary phosphate minerals whereas HREE are leached away as soluble complexes. The solubility of HREE is enhanced by the formation of more stable complexes such as carbonate, fluoride, oxalate (MICHARD et al., 1987; CANTRELL and BYRNE, 1987). Furthermore, H_2CO_3 is the most important aggressive agent in soil and can play a major role in the mobilization of HREE. This is emphasized by the syenite-normalized patterns of surface water (Fig. 12) which show a HREE-enrichment.

Behavior of Ce. The less weathered parent-rocks do not show a positive Ce-anomaly. In all the studied profiles on the Goyoum site as well as on the Akongo site, the positive Ce-anomaly is always located beneath the zone of iron oxide and oxihydroxide accumulation. These anomalies are independent of the parent rocks and the location results from differentiation within the profiles. Detailed study of the Ce distribution within the Akongo profile shows that the highest Ce contents and Ce anomalies are situated in the non-ferruginous seams and associated with the porosity of the white seams where halloysite needles precipitate. RANKIN and CHILDS (1976) observed, for some soils in New Zealand, that Ce anomalies (from 2 to 10) are related to the presence in soil of Fe-Mn concretions. Our study shows that it is not always the case and that iron and cerium can behave differently within lateritic environments.

Weathering of REE-bearing accessory minerals

Although the parent-rocks have REE contents around 150–300 ppm, the weathering processes lead to different Ce accumulations between the Akongo profile (up to 2000 ppm found within the accumulation zones) and the Goyoum profiles (up to 200 ppm). The difference is related to the influence of the primary LREE-bearing minerals on the mobilization of LREE. Allanite is the most important REE-bearing accessory mineral in the Akongo syenite whereas monazite is dominant in the Goyoum gneiss. PETIT et al. (1985) have

Table 4 : REE concentrations (ppb) of the pore-water and the two surface water samples from the Akongo marsh.

	Ce	Nd	Sm	Eu	Gd	Dy	Er	Yb
pore-water	6.10	1.75	0.28	0.02	-	-	-	-
marsh water 1	0.410	0.154	0.027	0.0072	0.019	0.014	0.0083	0.0083
marsh water 2	0.591	0.171	0.030	0.0076	0.020	0.015	0.0078	0.0072

shown that irradiation enhances the dissolution rate of the accessory minerals such as allanite and monazite. The dissolution kinetics of both minerals depend on metamictization processes. Metamictization is due to self-irradiation of the crystal, which leads to a disordering of the structure, therefore metamictization is proportional to (1) the U and Th contents of the crystals and (2) time. Although monazite contains more U and Th than allanite, the monazite crystals are not metamictized. Indeed, there is a healing of the crystal in which the lattice recovers its initial structure after alpha-recoil damage (EYAL and KAUFMAN, 1982). The Akongo syenite is Precambrian (800 Ma in age), and the great age allows sufficient time to damage extensively the allanite lattice, which results in rapid dissolution. Therefore the LREE from allanites from the Akongo profile can be mobilized and be either precipitated as phosphates or oxide (especially for Ce) or be leached away. In the Goyoum profiles, monazite remains as slightly weathered detrital grains. There is not enough leached LREE to produce Ce contents as high as those encountered in the Akongo profile.

In the Akongo profile, the fate of the REE depends strongly on the weathering kinetics of the REE-bearing minerals. The allanite and apatite crystals are broken down by hydrolysis. The $LREE^{3+}$ and PO_4^{3-} released from the dissolution of both species participate in the formation of secondary phosphates such as widespread florencite donuts according to the reaction:

$$2Ca_5[PO_4]_3F + 9Al^{3+} + 3LREE^{3+} + 18H_2O \rightarrow$$

fluorapatite

$$3Al_3LREE[PO_4]_2(OH)_6 + 10Ca^{2+} + 2F^- + 18H^+$$

florencite

In this reaction, apatite crystals are replaced by florencite donuts in the form of scattered donuts either isolated or in chains. It is important to point out that these donuts have no Ce-anomaly. Therefore, when LREE are incorporated into florencite crystals, Ce has the same behavior as the other REE.

The LREE content in groundwater depends on the equilibrium conditions between the florencite and the aqueous phase. The availability of LREE increases when allanite is more abundant than apatite within the parent rock.

The REE can remain in soil by adsorption on clay surfaces or take part in the growth of other REE-bearing crystals. The first mechanism is supported by works of several authors (ROALDSET, 1974; AAGAARD, 1974), who have clearly demonstrated that high REE concentrations in sedimentary clays are due to adsorption processes. The second mechanism is illustrated in an interesting experimental study (JONASSON et al., 1988), which shows that the adsorption of either HREE on crystalline LREE phosphates (monazite or rhabdophane), or LREE on crystalline HREE phosphate (xenotime) leads to the formation of new mineral phases on the phosphate surfaces such as HREE xenotime on monazite or LREE rhabdophane on xenotime.

The precipitation of CeO_2 and the mechanisms responsible for its concentration in the Akongo profile

Although trivalent cerium can be involved in the processes discussed above (incorporation within secondary minerals, adsorption on clay surfaces), the change in its oxidation state results in behavior different from that of the other REE. The presence of cerianite in the Akongo profile indicates that Ce occurs in its tetravalent state. In this profile, the positive Ce-anomalies are situated only within the saprolite and encountered in only two situations: the most important anomaly ($Ce/Ce^* = 10$) is located in some white clayey seams of the middle part of the saprolite (between 4 and 4.5 m deep) whereas the weaker anomalies ($Ce/Ce^* \leq 2$) occur in some sandy matrix samples from the top of the saprolite (Fig. 4).

The cerianite precipitation is interpreted as the result of the seasonal fluctuation of the groundwater table, which operates as a redox front. BILONG (1988) observed that the presence of a relatively impermeable basement induced the formation of a groundwater table and the flooding of the saprolite to the bottom of the mottled horizon during the wet periods (chiefly from March to July and from September to October).

The presence of the groundwater table has two main effects: (1) Flooding of the saprolite leads to the breakdown of the allanite and apatite crystals. Among the leached LREE, the major part is precipitated mainly as florencite, which is present in the saprolite. Another part can be adsorbed on clay surfaces. However the solution at equilibrium still contains REE at very low concentration, (2) flooding leads to anaerobic conditions which induce the mobility of certain cations in their low-valence state.

In order to understand the behavior of Ce under different redox conditions, we can compare Ce and Fe. The solution in equilibrium with the solid phases of the soil contains divalent iron and trivalent cerium. However, if the precipitated oxides are considered, cerium and iron behave differently; cerianite is found precipitated with halloysite in the clayey aggregates of the almost iron-oxide-free white seams.

The dynamics of the soil solution are controlled by the different pore distributions in the sandy matrix and in the seams. When the water level falls, the run-off of water in the very porous syenitic sand is probably much faster than in the clayey seams, where water remains a longer time in the smallest pores. When the groundwater has almost disappeared from the saprolite [i.e., at the beginning of the main dry season (from December to March)], water is retained only in the smallest pores of the saprolite and in the vicinity of the clayey seams. The largest pores of the saprolite contain soil atmosphere and especially CO_2 and O_2. During this period, water seepage and drainage probably takes place at the interface between clayey seams and the sandy matrix.

During this final phase of discharge and falling of the water table, water occurs only within the cracks and the pores of the seams. Ce and Fe behave differently in these domains. The Eh-pH diagram (Fig. 13), constructed with the data listed in Table 5, allows an explanation on the differential mechanisms. The diagram shows the stability fields of the cerianite (CeO_2) and goethite ($\alpha FeOOH$). The stability fields of Ce-lanthanite ($Ce_2(CO_3)_3 \cdot 8H_2O$) and siderite ($FeCO_3$) are also shown for $pP_{CO_2} = 3$. Goethite represents the stable iron hydroxide which directly precipitates in this lateritic soil. The boundaries between the solid phases and the soluble cations are drawn for an activity of 10^{-5} M for dissolved Fe^{2+} and activity ranges included between 10^{-6} and 10^{-9} M for Ce^{3+}. The order of magnitude of concentrations of Ce^{3+} and Fe^{2+} in groundwater have been chosen in accordance with the

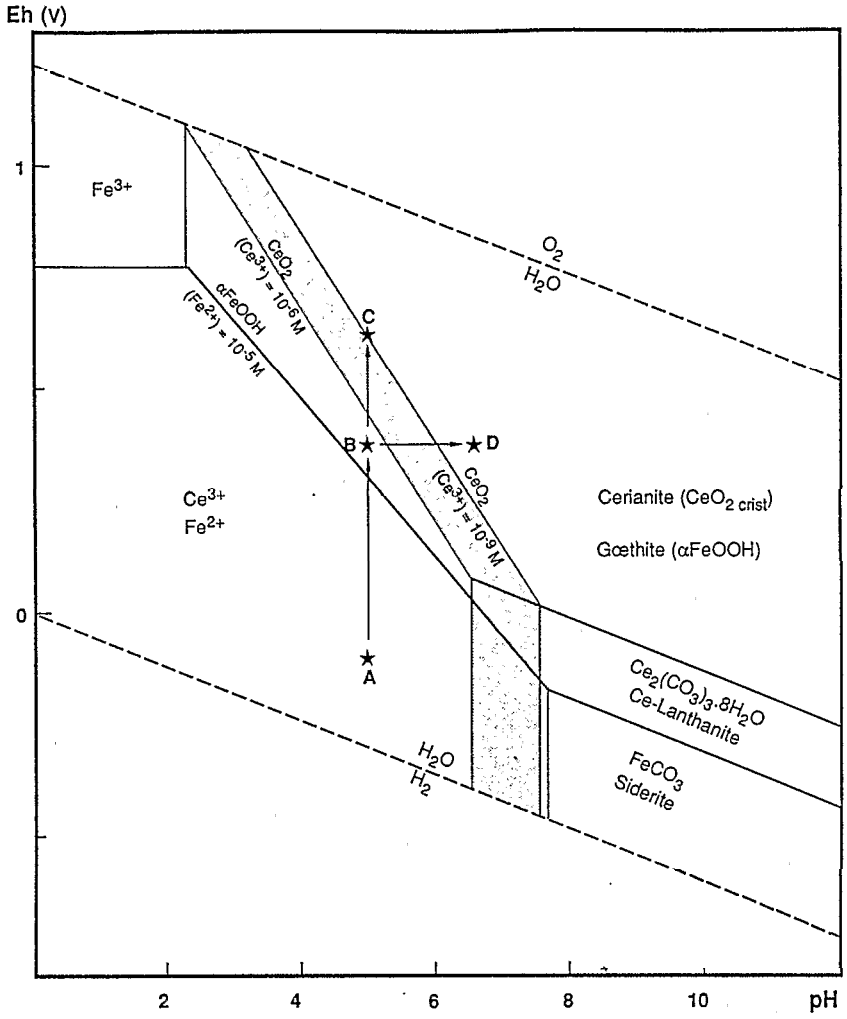

FIG. 13. Stability field of cerianite (CeO_2), Ce-lanthanide ($Ce_2(CO_3)_3 \cdot 8H_2O$), goethite ($\alpha FeOOH$), and siderite ($FeCO_3$) predicted from equilibrium constants log K_0 reported in Table 5. The range of the dissolved Ce^{3+} activity is included between 10^{-6} and 10^{-9} M, the activity of Fe^{2+} is 10^{-5} M, and $pP_{CO_2} = 3.0$. The speciation for both species are not taken into account.

analyses of the Akongo marsh water. Point A of Fig. 13 represents the redox conditions allowing the stability of Fe^{2+} and Ce^{3+} in soil solution at pH 5.0 and slightly negative Eh (about −0.1 V). When the water table falls, water is held at the interfaces between the clayey seams and the syenitic sand. If aerated conditions return in the sandy matrix, diffusion of O_2 into the water located at the interfaces will occur. An Eh increase will result, which will induce the precipitation of

Table 5 : Selected stability constants used to construct the simple stability field diagram (Fig. 13)

reactions	log K_0	
1) $Ce^{3+} + 2H_2O = CeO_2 + 4H^+ + e^-$	-21.32	(a)
2) $2Ce^{3+} + 3CO_2 + 11H_2O = Ce_2(CO_3)_3.8H_2O + 6H^+$	-17.96	(b)
3) $Fe^{2+} + 2H_2O = \alpha FeOOH + 3H^+ + e^-$	-14.89	(c)
4) $Fe^{2+} = Fe^{3+} + e^-$	-13.03	(d)
5) $Fe^{2+} + CO_2 + H_2O = FeCO_3 + 2H^+$	-7.46	(d)

(a) calculated from free energy data of SCHUMM et al. (1973) compiled by BROOKINS (1983).
(b) calculated from free energy data of ESSINGTON and MATTIGOD (1985).
(c) calculated from free energy data of TARDY and NAHON (1985).
(d) calculated from free energy data of ROSSINI et al. (1952) compiled by GARRELS and CHRIST (1965).

goethite (point B). The Fe^{2+} activity will decrease whereas the Ce^{3+} activity will remain unchanged. The precipitation of goethite as very fine coatings will occur on the walls of the white halloysitic seams and in their large fissural pores. When the soil solution is almost exclusively located in the pores of the seams and when the oxidizing conditions are maximum, Ce^{4+} will be precipitated as cerianite and fill up the aggregate pores, as shown on Fig. 7C.

After the main stage of oxidation which induces the goethite formation, there are various plausible ways of precipitating CeO_2: (1) A quick diffusion of O_2 in the water held by the aggregate pores can lead to the redox conditions of point C (Fig. 13) and (2) a rise in pH of the confined water, which could be caused by a decrease of the P_{CO_2} and an increase in the ionic strength of the solution, can lead to the cerianite precipitation without an Eh increase (point D).

In order to assess the water volume which must pass through the clayey white seams with an apparent density of about 1.8 g/cm^3 (to produce a 2000 ppm Ce content) the following assumptions can be considered: (1) The groundwater Ce content is the same as that of the reducing marsh sediment pore water (i.e., 6 μg/l), (2) all the groundwater cerium is precipitated, (3) the CeO_2 formation occurs after precipitation of secondary phosphates which do not indeed exhibit a Ce-anomaly, and (4) equilibrium conditions are realized. The result is a water/rock ratio of about 6.10^8 l/m^3.

CONCLUSIONS

1. Positive Ce-anomalies have been observed on chondrite-normalized REE patterns in four lateritic profiles from Cameroon. They are all located in the upper part of the saprolitic horizon beneath an iron oxide accumulation zone.
2. In the Akongo profile, where the Ce content is the highest (2000 ppm), it is shown that Ce is present as cerianite (CeO_2) which is coating halloysite needles in white clayey seams.
3. In this latter profile, the REE accessory minerals from the syenite (allanite, apatite, and sphene) are strongly weathered in the bottom of the saprolite and they have not been observed higher in the profile. Florencite and rhabdophane are newly-formed phases in the laterite.
4. Monazite, remaining in the Goyoum profile, is more resistant to strong weathering than allanite. Metamictization of allanite enhances the dissolution process.
5. Precipitation of cerianite at the top of the saprolite is due to the dynamics of the soil solution which, during the run-off of the water, induce oxygen transport into the pores of the clayey seams and the oxidation of Ce^{3+} to Ce^{4+}.

Acknowledgments—We are most grateful to the Yaoundé University staff and ORSTOM for facilitating the sampling at the Akongo site. The study on the Goyoum profiles has been supported by a C.E.A. (Commissariat à l'Energie Atomique) grant to Jean-Pierre Muller. Professor A. Herbillon is gratefully acknowledged for his thoughtful review of the manuscript. D. Nahon, W. S. Fyfe, J. I. Drever, and G. Sullivan are thanked for their reviews. Michel Doirisse, Jean-Marie Claude, Alain Kohler, and Françoise Elsass are thanked for their technical assistance with thin-plate preparation, electron microprobe analyses, and the scanning and transmission electron microscopy. This project has been partly supported by a DBT-INSU grant (AP 89/3828).

Editorial handling: J. I. Drever

REFERENCES

AAGAARD P. (1974) Rare earth elements adsorption on clay minerals. *Bull. Group. Franç. Argiles* **26,** 193–199.

DE BAAR H. J. W., GERMAN C. R., ELDERFIELD H., and VAN GAANS P. (1988) Rare earth element distributions in anoxic waters of the Cariaco Trench. *Geochim. Cosmochim. Acta* **52,** 1203–1219.

BALASHOV Y. A., RONOV A. B., MIGDISOV A. A., and TURANSKAYA N. V. (1964) The effect of climate and facies environment on the fractionation of the rare earths during sedimentation. *Geochem. Intl.* **10,** 951–969.

BILONG P. (1988) Génèse et développement des sols ferrallitiques sur syénite alcaline potassique en milieu forestier du centre-sud Cameroun. Comparaison avec les sols ferrallitiques développés sur roches basiques. Ph.D. dissertation, Univ. of Yaoundé.

BOCQUIER G., MULLER J. P., and BOULANGE B. (1984) Les latérites. Connaissances et perspectives actuelles sur les mécanismes de leur différenciation. In *Livre jubilaire de l'Association Française pour l'Etude du Sol* (ed. A.F.E.S.), pp. 123–138.

BONNOT-COURTOIS C. (1981) Géochimie des terres rares dans les principaux milieux de formation et de sédimentation des argiles. Ph.D. dissertation, Univ. of Orsay, Paris.

BROOKINS D. G. (1983) Eh-pH diagrams for the rare earth elements at 25°C and one bar pressure. *Geochem. J.* **17,** 223–229.

CANTRELL K. J. and BYRNE R. H. (1987) Rare earth element complexation by carbonate and oxalate ions. *Geochim. Cosmochim. Acta* **51,** 597–605.

DUDDY J. R. (1980) Redistribution and fractionation of rare earth and other elements in a weathering profile. *Chem. Geol.* **30,** 363–381.

EDIMO A. (1985) Le massif syénitique d'Akongo-Lolodorf (Sud-Cameroun). Interprétation des anomalies radiométriques. Comparaison avec l'arc syénitique Mont des Eléphant-Rocher du Loup. Ph.D. dissertation, Univ. of Orléans.

ELDERFIELD H. and SHOLKOVITZ E. R. (1987) Rare earth elements in the pore-waters of reducing nearshore sediments. *Earth Planet. Sci. Lett.* **82,** 280–288.

ELDERFIELD H., HAKWESWORTH G. H., and GREAVES M. J. (1981) Rare earth elements geochemistry of oceanic ferromanganese nodules and associated sediments. *Geochim. Cosmochim. Acta* **45,** 513–528.

ESSINGTON M. E. and MATTIGOD S. V. (1985) Lanthanide solid phase speciation. *Soil Sci. Soc. Amer. J.* **49,** 1387–1393.

EYAL Y. and KAUFMAN A. (1982) Alpha-recoil damage in monazite: preferential dissolution of the radiogenic actinide isotopes. *Nuclear Tech.* **58,** 77–83.

FRONDEL C. and MARVIN V. B. (1959) Cerianite, CeO_2, from Poços de Caldas, Brazil. *Amer. Mineral.* **44,** 882–884.

GARRELS R. M. and CHRIST C. L. (1965) *Solutions, Minerals and Equilibria.* Freeman, Cooper and Co., San Fransisco.

GOLDBERG E. D. (1961) Chemistry in the oceans. In *Oceanography* (ed. M. SHEARS), pp. 583–597. Amer. Assoc. Adv. Sci.

GOVINDARAJU K. and MEVELLE G. (1987) Fully automated dissolution and separation methods for inductively coupled plasma atomic emission spectrometry rock analysis. Application to the determination of rare earth elements. Plenary lecture. *J. Anal. Atomic. Spectr.* **2,** 615–621.

HESSLEIN R. H. (1976) An in-situ sampler for close internal pore-water studies. *Limnol. Oceanog.* **21,** 912–924.

HUMPHRIS S. E. (1984) The mobility of the rare earth elements in the crust. In *Rare Earth Element Geochemistry* (ed. P. HENDERSON), Chap. 9, pp. 317–340. Elsevier.

JONASSON R. G., BANCROFT G. M., and BOATNER L. A. (1988) Surface reaction of synthetic end-member analogues of monazite, xenotime and rhabdophane, and evolution of natural waters. *Geochim. Cosmochim. Acta* **52,** 767–770.

MICHARD A., ALBARÈDE F., MICHARD G., MINSTER J. F., and CHARLOU J. L. (1983) Rare earth elements and uranium in high temperature solutions from East Pacific Rise hydrothermal vent field (13°N). *Nature* **303**, 795–797.

MICHARD A., BEAUCAIRE C., and MICHARD G. (1987) Uranium and rare earth elements in CO_2-rich waters from Vals-les Bains (France). *Geochim. Cosmochim. Acta* **51**, 901–909.

MILLOT G. (1964) *Géologie des Argiles. Altérations, Sédimentologie, Géochimie.* MASSON, Paris.

MULLER J. P. (1987) Analyse pétrologique d'une formation latéritique meuble du Cameroun. Essai de traçage d'une différenciation supergène par les paragénèses minérales secondaires. Ph.D. dissertation, Univ. of Paris VII.

MULLER J. P. and BOCQUIER G. (1986) Dissolution of kaolinites and accumulation of iron oxides in lateritic-ferruginous nodules. Mineralogical and microstructural transformations. *Geoderma* **37**, 113–136.

NAHON D. (1987) Microgeochemical environments in laterite weathering. In *Symp. on Geochem. of the Earth Surface and processes of Minerals Formation, Grenada, 1986*, (eds. R. RODRIGUEZ-CLEMENTE and Y. TARDY), pp. 141–156. Consejo Superior Investigaciones Cientificas, Madrid.

NESBITT H. W. (1979) Mobility and fractionation of rare earth elements during weathering of a granodiorite. *Nature* **279**, 206–210.

PETIT J. C., LANGEVIN Y., and DRAN J. C. (1985) Radiation-enhanced release of uranium from accessory minerals in crystalline rocks. *Geochim. Cosmochim. Acta* **49**, 871–876.

PIPER D. Z. (1974) Rare earth elements in ferromanganese nodules and other marine phases. *Geochim. Cosmochim. Acta* **29**, 1007–1022.

POUCHOU J. L. and PICHOIR F. (1984) Un nouveau modèle de calcul pour la microanalyse quantitative par spectrométrie de rayons X. *La Recherche Spatiale* **3**, 167–192.

RANKIN P. C. and CHILDS C. W. (1976) Rare earth elements in iron-manganese concretions from some New Zealand soils. *Chem. Geol.* **18**, 54–64.

ROALDSET E. (1974) Lanthanide distributions in clays. *Bull. Group. Franç. Argiles* **26**, 201–209.

RONOV A. B., BALASHOV Y. A., and MIGDISOV A. A. (1967) Geochemistry of the rare earths in the sedimentary cycle. *Geochem. Intl.* **4**, 1–17.

ROSSINI F. D., WAGMAN D. D., EVANS W. H., LEVINE S., and JAFFE I. (1952) Selected values of chemical thermodynamic properties. *Natl. Bur. Standards Circ. 500.* US Dept. Commerce.

SARAZIN G., FOUILLAC C., MICHARD G. (1976) Etude de l'acquisition d'éléments dissous par les eaux de lessivage des roches granitiques sous climats tempéré. *Geochim. Cosmochim. Acta* **40**, 1481–1486.

SARAZIN G., ILDEFONSE P., and MULLER J. P. (1982) Contrôle de la solubilité du fer et de l'aluminium en milieu ferrallitique. *Geochim. Cosmochim. Acta* **46**, 1267–1279.

SAWKA W. N., BANFIELD J. F., and CHAPPELL B. W. (1986) A weathering-related origin of widespread monazite in S-type granites. *Geochim. Cosmochim. Acta* **50**, 171–175.

SHUMM R. M., WAGMAN D. D., BAILEY S. M., EVANS W. H., and PARKER V. B. (1973) Selected values of chemical thermodynamic properties. Table for the lanthanide elements (elements 62 through 76 in the standard order arrangement). *USA Natl. Bur. Standards Tech. Note 270.7.*

STEINBERG M. and COURTOIS C. (1976) Le comportement des terres rares au cours de l'altération et ses conséquences. *Bull. Soc. Geol. France* **1**, 13–20.

STYLES N. T. and YOUNG B. R. (1983) Fluocerite and its alteration products from the Afu Hills, Nigeria. *Mineral. Mag.* **47**, 41–46.

TARDY Y. and NAHON D. (1985) Geochemistry of laterites. Stability of Al-gœthite, Al-hematite and Fe^{3+}-kaolinite in bauxites and ferricretes. An approach to the mechanism of concretion formation. *Amer. J. Sci.* **285**, 865–903.

TOPP S. E., SALBU B., ROALDSET E., and JORGENSEN P. (1984) Vertical distribution of trace elements in laterite soil (Suriname). *Chem. Geol.* **47**, 159–174.

TRESCASES J. J., FORTIN P., MELFI A., and NAHON D. (1986) Rare earth elements accumulation in lateritic weathering of Pliocene sediments, Curitiba basin (Brazil). In *Proc. Intl. Meeting Geochem. Earth Surface and Process of Mineral Formation,* pp. 260–271.